Article

Robustness of post-reconstruction and direct kinetic parameter estimates under rigid head motion in dynamic brain PET imaging

KOTASIDIS, F.A., *et al*.

Physica Medica 53 (2018) 40–55

Contents lists available at ScienceDirect

Physica Medica

journal homepage: www.elsevier.com/locate/ejmp

Original paper

Robustness of post-reconstruction and direct kinetic parameter estimates under rigid head motion in dynamic brain PET imaging

F.A. Kotasidis[a,b], G.I. Angelis[c], J.M. Anton-Rodriguez[b], H. Zaidi[a,d,e,f,*]

[a] Division of Nuclear Medicine and Molecular Imaging, Geneva University Hospital, CH-1211 Geneva, Switzerland
[b] Wolfson Molecular Imaging Centre, MAHSC, University of Manchester, M20 3LJ Manchester, UK
[c] Faculty of Health Sciences, Brain and Mind Centre, The University of Sydney, NSW 2050 Sydney, Australia
[d] Geneva Neuroscience Centre, Geneva University, CH-1205 Geneva, Switzerland
[e] Department of Nuclear Medicine and Molecular Imaging, University of Groningen, University Medical Centre Groningen, 9700 RB Groningen, The Netherlands
[f] Department of Nuclear Medicine, University of Southern Denmark, DK-500 Odense, Denmark

ARTICLE INFO

Keywords:
PET
Brain imaging
Head motion
Kinetic modelling
Parameter estimation

ABSTRACT

Objective: Dynamic PET imaging is extensively used in brain imaging to estimate parametric maps. Inter-frame motion can substantially disrupt the voxel-wise time-activity curves (TACs), leading to erroneous maps during kinetic modelling. Therefore, it is important to characterize the robustness of kinetic parameters under various motion and kinetic model related factors.

Methods: Fully 4D brain simulations ($[^{15}O]H_2O$ and $[^{18}F]$FDG dynamic datasets) were performed using a variety of clinically observed motion patterns. Increasing levels of head motion were investigated as well as varying temporal frames of motion initiation. Kinetic parameter estimation was performed using both post-reconstruction kinetic analysis and direct 4D image reconstruction to assess bias from inter-frame emission blurring and emission/attenuation mismatch.

Results: Kinetic parameter bias heavily depends on the time point of motion initiation. Motion initiated towards the end of the scan results in the most biased parameters. For the $[^{18}F]$FDG data, k_4 is the more sensitive parameter to positional changes, while K_1 and blood volume were proven to be relatively robust to motion. Direct 4D image reconstruction appeared more sensitive to changes in TACs due to motion, with parameter bias spatially propagating and depending on the level of motion.

Conclusion: Kinetic parameter bias highly depends upon the time frame at which motion occurred, with late frame motion-induced TAC discontinuities resulting in the least accurate parameters. This is of importance during prolonged data acquisition as is often the case in neuro-receptor imaging studies. In the absence of a motion correction, use of TOF information within 4D image reconstruction could limit the error propagation.

1. Introduction

Dynamic positron emission tomography (PET) is extensively used in neuro-receptor and brain imaging to probe a number of functional aspects of the living brain. Following data acquisition, the time course of the activity distribution can be modelled to derive pharmacokinetic parameters related to metabolism, blood flow, oxygen utilization and different aspects of neurotransmission amongst others. Due to the long data acquisition lasting frequently over 1.5 h, voluntary and involuntary, inter- as well as intra- frame head motion can significantly affect and distort the regional and voxel-wise time activity curves (TACs). Voluntary motion occurs as a result of the patient taking a new posture to alleviate aches and pressure points from prolonged positioning to an uncomfortable posture (mostly young children in paediatric PET and elderly people), interacting with scanning personnel (during injection, moving feet to new position or positioning of a feet or other rest, talking) or in response to a verbal or other activation paradigm (speech tasks or movement of extremities). On the other hand, involuntary movements involve slow as well as rapid changes in the head posture. Slow changes are often caused by the subject gradually relaxing as the scan progresses, or even falling asleep and can account for translations in excess of 15 mm due to the head slowly drifting. Rapid involuntary changes in the head posture can be caused by sneezing, coughing or instinctively responding to unexpected external stimuli. On top of that, such rapid movements can be originating from the pathology of the subject, such as in patients with Tourette

* Corresponding author at: Division of Nuclear Medicine and Molecular Imaging, Geneva University Hospital, CH-1211 Geneva, Switzerland.
E-mail address: habib.zaidi@hcuge.ch (H. Zaidi).

https://doi.org/10.1016/j.ejmp.2018.08.006
Received 2 August 2017; Received in revised form 6 August 2018; Accepted 7 August 2018
Available online 15 August 2018

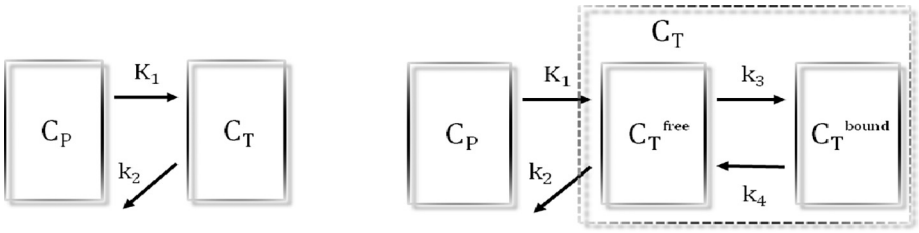

Fig. 1. Schematic diagram of a single-tissue and a two-tissue kinetic model showing the different compartments as well as the constant rate controlling the rate of change in activity concentration for each compartment.

Table 1
Simulated motion patterns for the dynamic [^{15}O]H_2O study.

	Early frames	Middle frames	Late frames
High frequency movement – permanent new position	1°, 2° and 4° around x-axis at the 7th frame [30 sec]	*No motion*	*No motion*
High frequency movement – permanent new position	*No motion*	1°, 2° and 4° around x-axis at the 16th frame [80 sec]	*No motion*
High frequency movement – permanent new position	*No motion*	*No motion*	1°, 2° and 4° at the 25th frame [240 sec]
High frequency movement – return to original position	2° around the x-axis at the 7th frame [30 sec], −2° around the x-axis at the 13th frame [60 sec]	*No motion*	*No motion*
High frequency movement – return to original position	*No motion*	2° around the x-axis at the 16th frame [80 sec], −2° around the x-axis at the 18th frame [100 sec]	*No motion*
High frequency movement – return to original position	*No motion*	*No motion*	2° around the x-axis at the 25th frame [240 sec], −2° around the x-axis at the 27th frame [300 sec]
Continuous drift	1° around the x-axis at the 7th frame [30 sec] and at the 13th frame [60 sec]	1° around the x-axis at the 18th frame [100 sec] and at the 24th frame [210 sec]	1° around the x-axis at the 27th frame [300 sec]
Simulated clinical case 1	Multiple frames with maximum rotations and translations of up to 6.2° and 19 mm		
Simulated clinical case 2	Multiple frames with maximum rotations and translations of up to 4° and 4.1 mm		

syndrome, Parkinson or epilepsy [1–6].

Methods to minimize potential head motion include the use of head immobilization and restraining equipment (thermoplastic masks, forehead and chin velcro restrains, stereotactic head fixation). However, such equipment, depending on the rigidity of the fixation, could also contribute to additional movement as the subject could try to alleviate pressure points and aches. Furthermore, some fixations cannot always be tolerated, especially by elderly patients and often those presenting neurological/psychiatric disorders. Therefore, a number of approaches were proposed to continuously track and subsequently correct for head motion if needed [7]. These can be divided into projection-based techniques [4,8–12] and post-reconstruction or image-based techniques [13–17]. However, image-based techniques for frame-by-frame transformations are usually tracer/activity dependent and susceptible to noise (especially in early frames). They also suffer from problems related to rigid marker fixation when optical devices are used. Alternatively, projection-based approaches can be more computationally intensive and slow to converge, have difficulties to handle out-of-field-of-view (FOV) events and are limited by the optical tracking device accuracy. Therefore, in cases where no motion correction is used or residual errors remain due to the shortcomings of the selected motion correction scheme, the errors introduced by either emission/attenuation mismatch, intra- and inter-frame motion blurring, or both, could lead to kinetic parameter errors. Motion-induced errors can substantially reduce the spatial resolution in parametric images. This is particularly of importance given that parametric maps are preferred over regional kinetic analysis when probing information from small brain structures, since they can provide kinetic parameters at the voxel level. However, even more important is that sudden changes between temporal frames can generate severe discontinuities in time-activity curves (TACs), therefore resulting in highly biased kinetic parameters especially at the boundaries of regions with high activity and attenuation gradients [8,18,19]. The impact of head rotations and translations on kinetic parameters has been previously investigated for specific tracers and for varying levels of motion [19,20]. However, given the fact that certain parameters are derived from certain parts of the TACs, some are expected to be more robust to a given motion pattern than others. This would depend not only on the magnitude of motion but also on the time when it occurs relative to the beginning of the scan and the kinetic model order (number of compartments and kinetic parameters) used. Furthermore, motion-induced errors might be different amongst kinetic parameter estimation methods. Direct parameter estimation methods have been shown to generate parametric images of improved accuracy and precision when used in brain imaging applications [21–23]. However, it has also been shown that when used in body imaging, motion-induced kinetic parameter errors tend to spatially propagate in the FOV during parameter estimation [24]. Therefore, it is of importance to investigate their behaviour in dynamic brain imaging given the different nature and magnitude of motion compared to abdominal imaging, as such algorithms have been consistently shown to supersede traditional post-reconstruction kinetic modelling approaches.

In this work, we systematically investigate the robustness of kinetic parameters against head motion in dynamic brain imaging using motion rotations and translations of varying amplitude and at different time points.

Both 1-tissue and 2-tissue kinetic models are used based on [^{18}F]FDG and [^{15}O]H_2O kinetics. In addition, we performed realistic simulations based on externally tracked motion data recorded during patient dynamic scans. Kinetic parameter estimation was performed using both post-reconstruction kinetic analysis as well as direct 4D image reconstruction.

2. Methods

2.1. Simulated dynamic datasets

To investigate the robustness of kinetic parameters against head motion, fully 4D dynamic datasets were generated using a digital brain phantom based on the Hammersmith atlas [25,26]. Two dynamic PET protocols were simulated corresponding to typical dynamic brain [^{15}O]H_2O and [^{18}F]FDG scanning sessions, representing a 1-tissue and a 2-tissue models (model order 1 and 2, respectively) (Fig. 1). For the [^{15}O]H_2O protocol, TACs were generated using a 1-tissue 3 parameter model (K_1, k_2, blood volume). A 360 s total scan duration was selected, re-binned into 28 frames [14 × 5 s, 5 × 10 s, 3 × 20 s, 6 × 30 s]:

$$C_T = IRF\,(K_1, k_2, t) \otimes \; C_P + bvC_p = K_1 e^{-k_2 t} \otimes \; C_p + bvC_p \tag{1}$$

For the [^{18}F]FDG protocol, TACs were generated using a 2-tissue model 5 parameter model assuming reversible kinetics during the course of the scan and including also a blood volume component (K_1, k_2, k_3, k_4 and blood volume). A 3300 s total scan duration was chosen, rebinned into 29 frames [9 × 10 s, 3 × 30 s, 4 × 60 s, 4 × 120 s, 8 × 300 s]:

$$\begin{aligned} C_T &= IRF\,(K_1, k_2, k_3, k_4, t) \otimes \; C_P + bvC_p \\ &= \frac{K_1}{(a_2 - a_1)}[(k_3 + k_4 - a_1)e^{-a_1 t} + (a_2 - k_3 - k_4)e^{-a2t}] \otimes \; C_p + bvC_p \end{aligned} \tag{2}$$

$$a_1 = \frac{(k_2 + k_3 + k_4) - \sqrt{(k_2 + k_3 + k_4)^2 - 4k_2k_4}}{2},\; a_2 = \frac{(k_2 + k_3 + k_4) + \sqrt{(k_2 + k_3 + k_4)^2 - 4k_2k_4}}{2} \tag{3}$$

where C_T and C_P is the tissue and plasma activity concentrations and bv the blood volume. Frame duration and number of frames were optimized and are representative of the parameters used in the standard of care dynamic FDG and $^{15}H_2O$ scans. For both FDG and $^{15}H_2O$ simulated data, the input functions were taken from patient derived arterial blood sampling data. The same input function was used for generating the simulated time activity curves and for kinetic modelling. The anatomical information of the digital phantom were generated based on a brain atlas consisting of 83 regions. To assign kinetic parameters to each region, patient brain scans were analyzed to estimate voxel-wise kinetic parameters. Subsequently, voxel-wise kinetic parameters were extracted for each region, following registration to the brain atlas, which were then averaged and uniformly assigned to each of the 83 corresponding regions in the phantom. Using the regionally averaged parameters and the operational equations presented in Eqs. (1) and (2), dynamic data were simulated for each region and for both kinetic models.

2.2. Simulated head motion

Fifteen different scenarios were investigated for each of the 2 kinetic models with different motion patterns during the course of a dynamic scan. Three different rotation levels at 1°, 2° and 4° around the x-axis (most commonly encountered during a scan) were simulated with the patient moving permanently to the new position [27]. The situation where the patient returned to the original position after some time had elapsed was also simulated for the 2° rotation. Each of these rotations were simulated to occur at 3 different time points relative to the start of the scan, with the time points varying between the 2 tracers due to the large difference in total scanning time between the [^{15}O]H_2O and the [^{18}F]FDG scan protocols. Apart from high frequency sudden moves, the case of slow head drift was also simulated with a total rotation of 5° around the x-axis occurring at 1° steps at different time points during the scan. Finally, 2 cases were simulated representing realistic head rotations and translations at varying severity during neuro-receptor imaging studies as acquired on the HRRT scanner. The transformation parameters simulated were estimated following frame-by-frame registration using the automated image registration (AIR) software [28]. To improve registration accuracy post-smoothed non-attenuation corrected images were used, thus enabling rigid-body registration between dynamic frames by neglecting motion in the early frames [29]. The accuracy of registration was checked visually and was found to be satisfactory. This might not be the optimal approach but it worked fine and was sufficient for our study. Table 1 summarizes the motion patterns that were used, while Fig. 2 shows simulated noiseless [^{15}O]H_2O and [^{18}F]FDG TACs from the substantia nigra in the central part of the brain, for each simulated motion pattern. The corresponding attenuation maps were also based on the brain atlas (gray and white matter's linear attenuation coefficient = 0.096 cm^{1}). To decouple the effect of inter-frame motion on kinetic parameters from emission-transmission mismatch, 2 cases were investigated. In the first case, the simulated attenuation maps were motion matched to the emission data during forward projection and subsequent reconstruction, hence only inter-frame motion was simulated. For that purpose, the attenuation map was rotated and translated according to the corresponding emission data for each individual frame. In the second case, the combined impact of inter-frame motion and emission/transmission mismatch was simulated. For that purpose, the emission data at each temporal frame were attenuated during forward projection using the corresponding motion-matched attenuation map but attenuation corrected during image reconstruction using the attenuation map corresponding to the reference motion-free state. Table 2

2.3. Projection data generation, image reconstruction and kinetic modelling

An in-house analytical simulator was used to generate the projection data. The analytical simulator used in this work is similar to the one implemented in the STIR package[1] enabling to forward project emission PET data considering photon attenuation effects and adding representative noise level. The dynamic emission images for each head motion pattern and time frame along with the corresponding attenuation images were forward projected onto a virtual scanner corresponding to the geometry configuration of the mCT PET/CT scanner (Siemens Healthcare, Erlangen, Germany) [30]. Randoms and scatter events were not considered while noiseless data were considered to investigate the motion effects on parameter bias. Furthermore, Poisson noise was also introduced in the projection data corresponding to representative cases from each motion pattern (4° rotation, continuous drift and clinical cases). Dynamic projection data were reconstructed using traditional 3-D image reconstruction (3D OP-OSEM up to 10 iterations [21 subset]) as well as using direct 4D image reconstruction (4D OP-OSEM up to 10 iterations [21 subset]). The direct 4D TOF reconstruction was based on an EM-based direct 4D framework, which allows separation between the tomographic and kinetic modelling steps [31]. This algorithm, is based on solving the spatiotemporal 4D maximum likelihood problem in projection space,

$$\alpha^{opt} = \arg\max_{\alpha} \sum_{il} (m_{il}\log_e(y_{il}) - y_{il}) \tag{4}$$

$$y_{il} = \sum_j p_{ij}\lambda_{jl} + \eta_{il} = \sum_j p_{ij} f_{jl}(\alpha) + \eta_{il} \tag{5}$$

where during the lth time frame and in the ith data bin, m_{il} are the PET measured data, y_{il} the mean number of events, η_{il} the mean number of erroneous events, p_{ij} the probability system matrix of a photon emitted from the jth voxel and being detected in the ith projection bin and λ_{jl} is the number of emissions from the jth voxel in the image during the lth time frame described by a kinetic model f_{jl} with parameter vector ;; into

[1] http://stir.sourceforge.net/

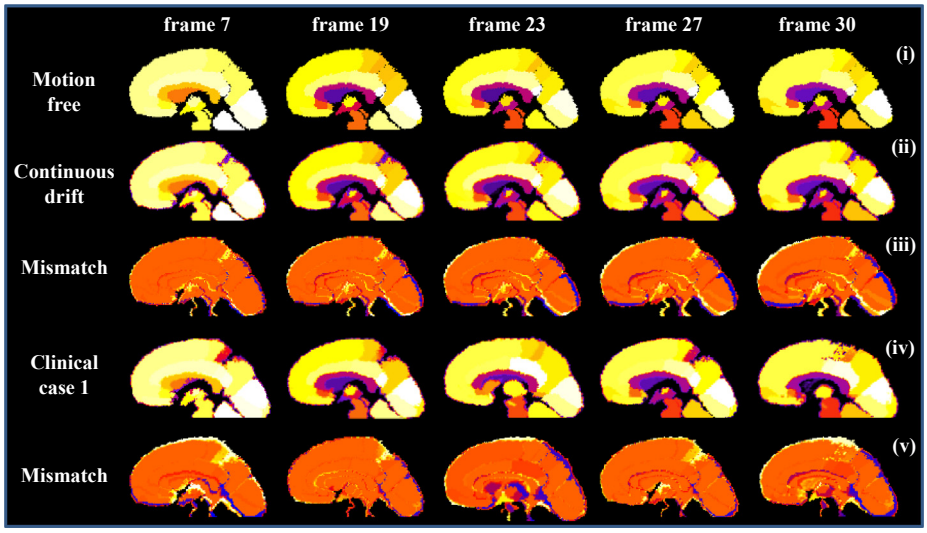

Fig. 2. Simulated dynamic brain data from 5 representative frames without motion (i), for the case of simulating a continuous drift (5 rotations of 1° on each of the depicted frames) as well as for one of the simulated clinical cases, along with the corresponding respective mismatch to the motion-free data (iii, v). In the continuous drift case, the mismatch to the motion free state for each corresponding frame becomes progressively larger as the head progressively rotates around the pivot point in a controlled way, simulating the head relaxing during the course of the scan. In the simulated clinical case, both rotations and translations were simulated based on measured motion during a dynamic HRRT brain scan.

Table 2
Simulated motion patterns for the dynamic [^{18}F]FDG study.

	Early frames	Middle frames	Late frames
High frequency movement – permanent new position	1°, 2° and 4° around the x-axis at the 7th frame [30 sec]	*No motion*	*No motion*
High frequency movement – permanent new position	*No motion*	1°, 2° and 4° around the x-axis at the 22th frame [470 sec]	*No motion*
High frequency movement – permanent new position	*No motion*	*No motion*	1°, 2° and 4° at 30th frame [2690 sec]
High frequency movement – return to original position	2° around the x-axis at the 7th frame [30 sec], −2° around the x-axis at the 14th frame [70 sec]	*No motion*	*No motion*
High frequency movement – return to original position	*No motion*	2° around the x-axis at the 22nd frame [470 sec], −2° around the x-axis at the 24th frame [890 sec]	*No motion*
High frequency movement – return to original position	*No motion*	*No motion*	2° around the x-axis at the 30th frame [2690 sec], −2° around the x-axis at the 32nd frame [3290 sec]
Continuous drift	1° around the x-axis at the 7th frame [30 sec] and at the 19th frame [230 sec]	1° around the x-axis at the 23rd frame [590 sec] and at the 27th frame [1790 sec]	1° around the x-axis at the 30th frame [2690 sec]
Simulated clinical case 1	Multiple frames with maximum rotations and translations of up to 6.2° and 19 mm		
Simulated clinical case 2	Multiple frames with maximum rotations and translations of up to 4° and 4.1 mm		

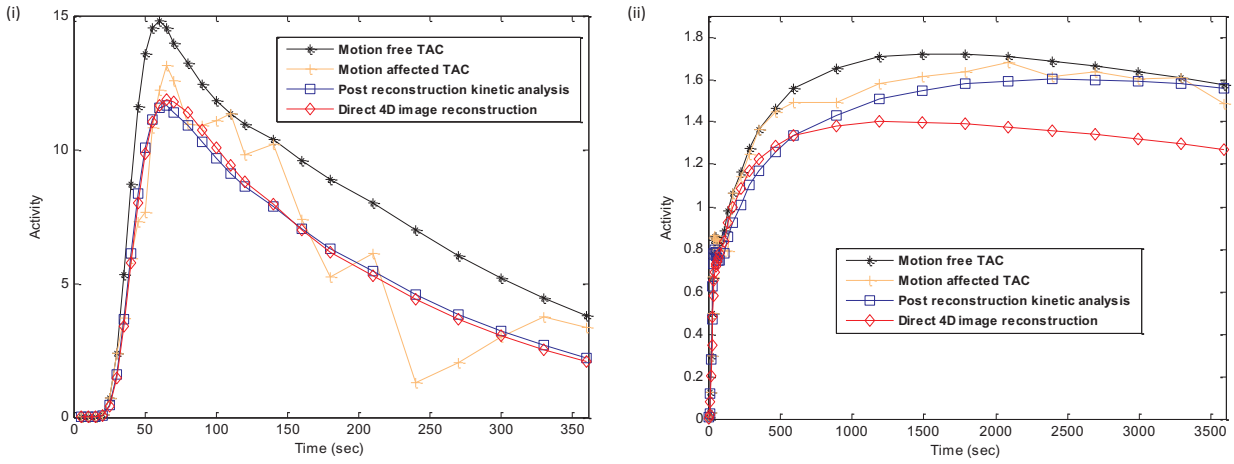

Fig. 3. Representative simulated and fitted regional time-activity curves from the amygdala both for 1-tissue ([^{15}O]H_2O) (i) and 2-tissue ([^{18}F]FDG) (ii) models. Data are shown for the severe simulated clinical motion pattern (10 iterations [21subsets]).

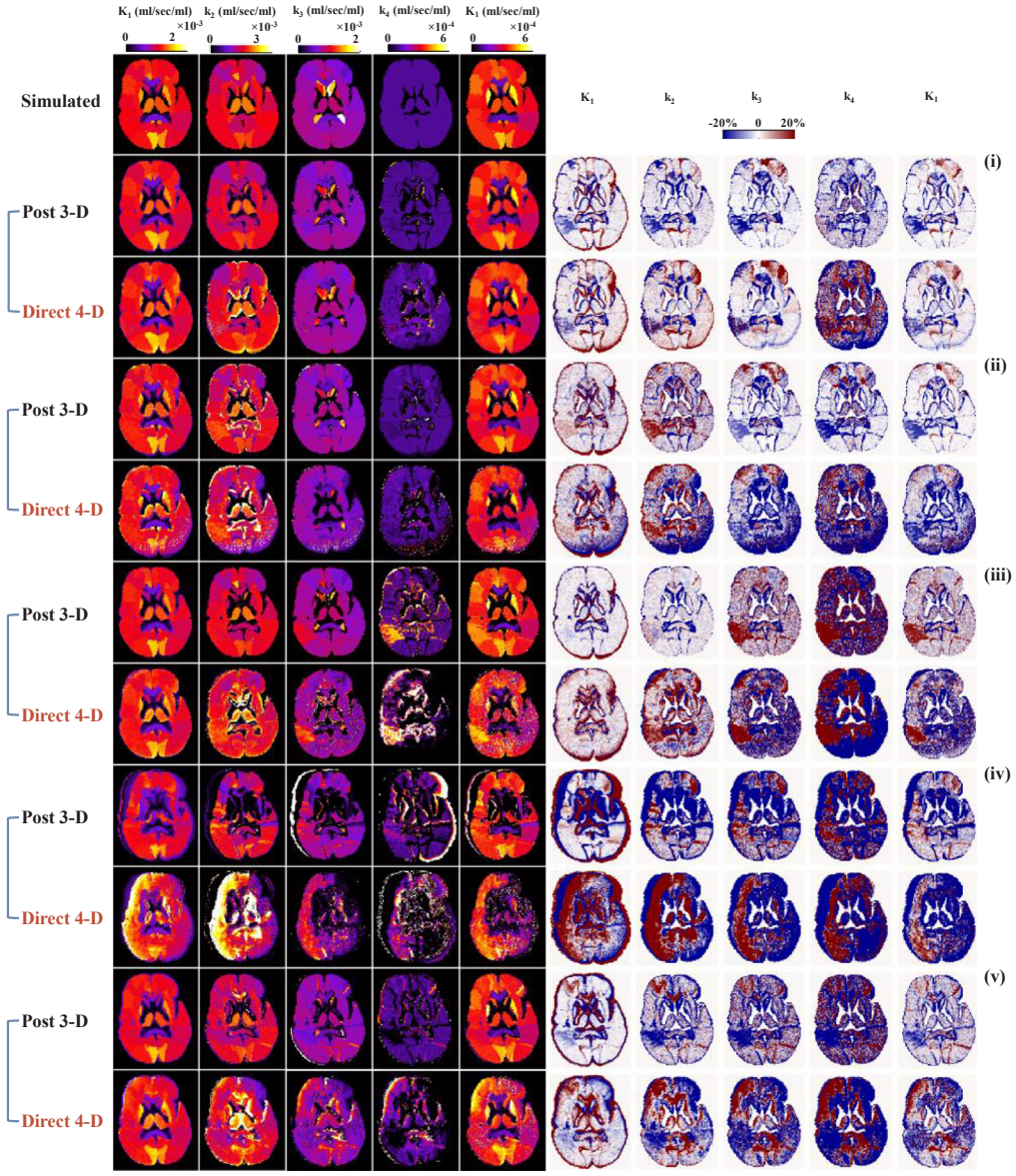

Fig. 4. Simulated and estimated kinetic parameters from noiseless data along with the corresponding bias parametric maps for a representative slice through the [^{18}F]FDG brain phantom. Parameters were estimated both with post-reconstruction kinetic analysis and direct 4D image reconstruction and correspond to early (i), middle (ii) and late frame (iii) motion with a 4-degree rotation, as well as a representative severe (iv) and mild (v) patient motion pattern.

a maximum likelihood problem in image space

$$\alpha^{(k+1)} = \arg\max_{\alpha} \sum_{j} \left(\sum_{i} p_{ij} \right) \sum_{l} \left(\lambda_{jl}^{(k+1)} \log_e(f_{jl}(\alpha)) - f_{jl}(\alpha) \right) \tag{6}$$

where

$$\lambda_{jl}^{(k+1)} = \frac{f_{jl}(\alpha^{(k)})}{\sum_{i} p_{ij}} \sum_{i} \frac{p_{ij} y_{il}}{\sum_{j'} p_{ij'} f_{j'l}(\alpha^{(k)}) + \eta_{il}} \tag{7}$$

Using a one-step late approach, Eq. (6) can be approximated with a weighted least square problem:

$$\alpha^{(k+1)} = \arg\min_{\alpha} \frac{1}{2} \sum_{jl} w_{jl}(\alpha) (\lambda_{jl}^{(k+1)} - f_{jl}(\alpha))^2 \tag{8}$$

with k being the number of iterations.

The algorithm proceeds by alternating between the tomographic EM image update (Eq. (7)) and the voxelwise image-based least squares kinetic modelling steps (Eq. (8)).

Kinetic parameter estimation for both post-reconstruction kinetic analysis and direct image reconstruction was based on the generalized linear least square (GLLS) method (2 internal iterations for 1-tissue model [^{15}O]H_2O data and 4 iterations for the 2-tissue model [^{18}F]FDG data) while the linear least square (LLS) method was used to initialize the kinetic parameters for GLLS [32]. The dynamic [^{15}O]H_2O data were modelled using a 2 parameter model as well as a blood volume component (K_1, k_2 and bv) while the [^{18}F]FDG data were modelled using a 4 parameter model using also a blood volume component (K_1, k_2, k_3, k_4 and bv) (see Supplementary Tables s1 & s2).

3. Results

3.1. Noiseless data

Representative simulated and fitted regional time-activity curves (amygdala) from the [^{15}O]H_2O and [^{18}F]FDG datasets are shown in Fig. 3 for the severe simulated motion. For the [^{18}F]FDG data, there is a clear differentiation between the post-reconstruction and direct 4D fitted TACs with the late frames in the latter exhibiting increased

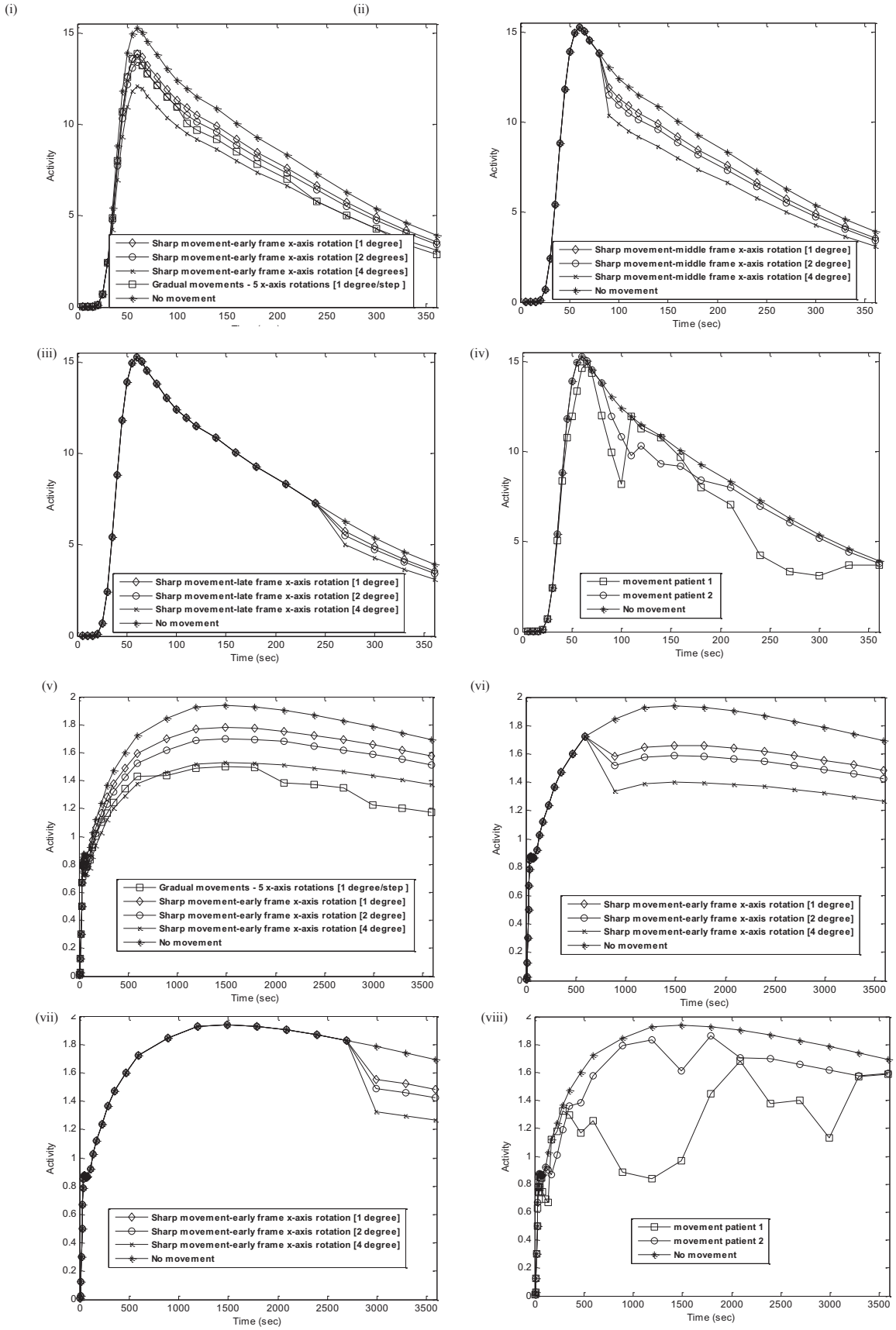

Fig. 5. Simulated regional TACs from the substantia nigra for both 1-tissue ($[^{15}O]H_2O$) (i-iv) and 2-tissue ($[^{18}F]FDG$) (v-viii) models. Representative TACs are shown for early (i, v), middle (ii, vi), and late (iii, vii) frame movements as well as for the simulated clinical cases (iv, viii). The simulated continuous slow drift is also shown (i, v) while the motion free case is also visible for comparison.

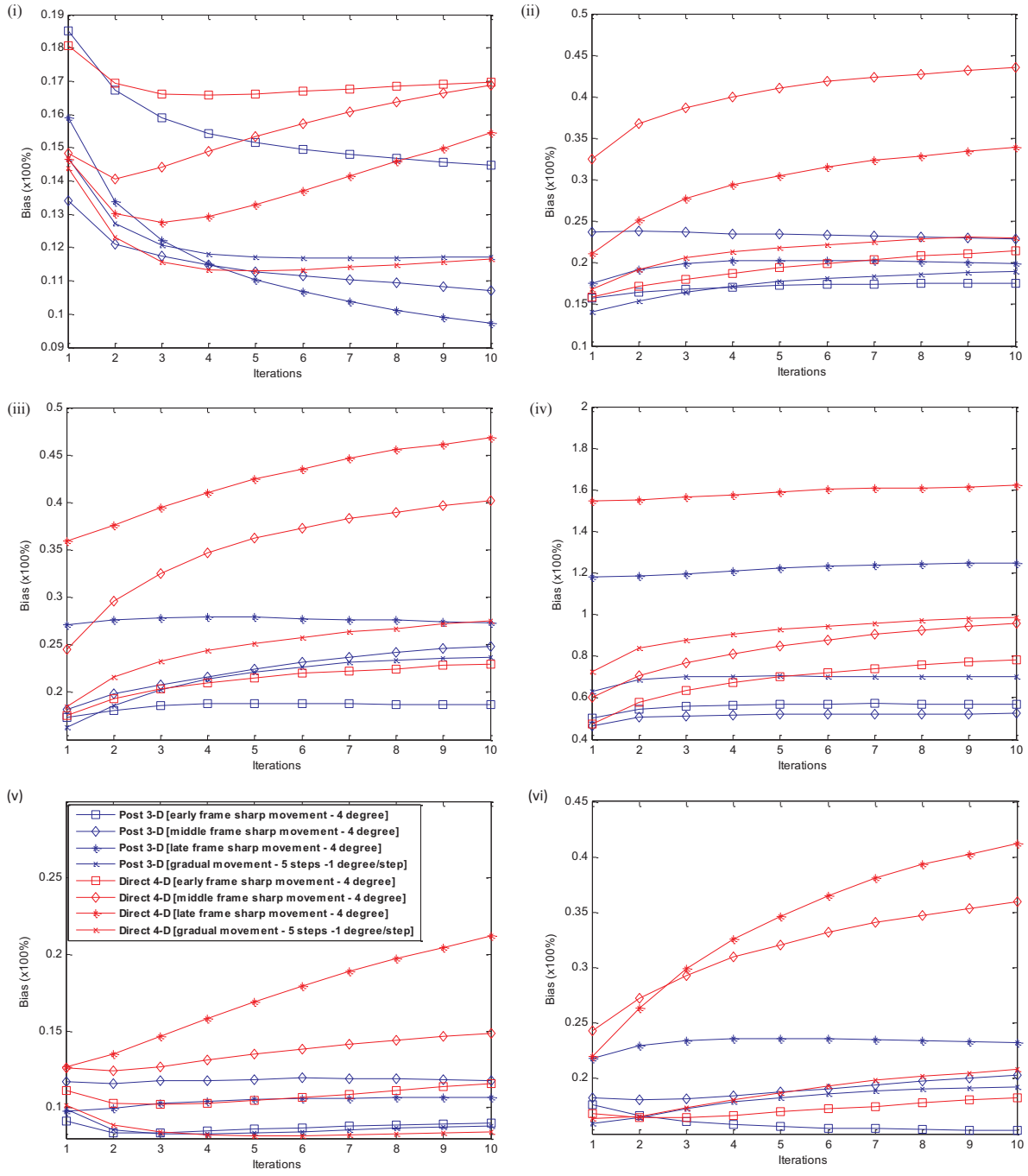

Fig. 6. Whole brain kinetic parameter bias from [^{18}F]FDG noiseless data for K_1 (i), k_2 (ii), k_3 (iii), k_4 (iv), blood volume (v) and K_i (vi) at high levels of early, middle and late frame motion as well as during slow continuous drift. Parameters are estimated both with post-reconstruction kinetic analysis and direct 4D image reconstruction.

negative bias up to ~25%. On the other hand, post-reconstruction fitting, even though resembling the direct 4D fit in the early frames (where there is reduced motion) and is similarly biased, it is able to more closely match the simulated amygdala TAC. On the [^{15}O]H_2O data, both parameter estimation methods appear to be similarly negatively biased with small differences between them.

3.1.1. 2-tissue model

Parametric maps for all simulated motion patterns were generated following model fitting, using both post-reconstruction analysis and direct 4D reconstruction. Fig. 4 shows the estimated kinetic parameters from the [^{18}F]FDG datasets along with the corresponding parametric bias maps for a subset of the simulated motion patterns. Looking at the 3 sudden motion patterns with respect to when motion occurred (Fig. 4(i–iii)), it is apparent that different parameters are affected to a different degree depending on the temporal occurrence of motion. When parameters are estimated post-reconstruction, early frame motion appears to affect all parameters mildly while motion occurring in the middle frames results in an increased k_2 bias. When motion occurs late during the scan, k_3 and k_4 appear to be more susceptible to changes in the TAC. Finally, in both clinically observed simulated motion cases, all parameters appear heavily biased with the least biased parameters being K_1 probably due to the fact that motion in the early stages of the scan is less severe. As can be seen in the simulated TACs (Fig. 5), one

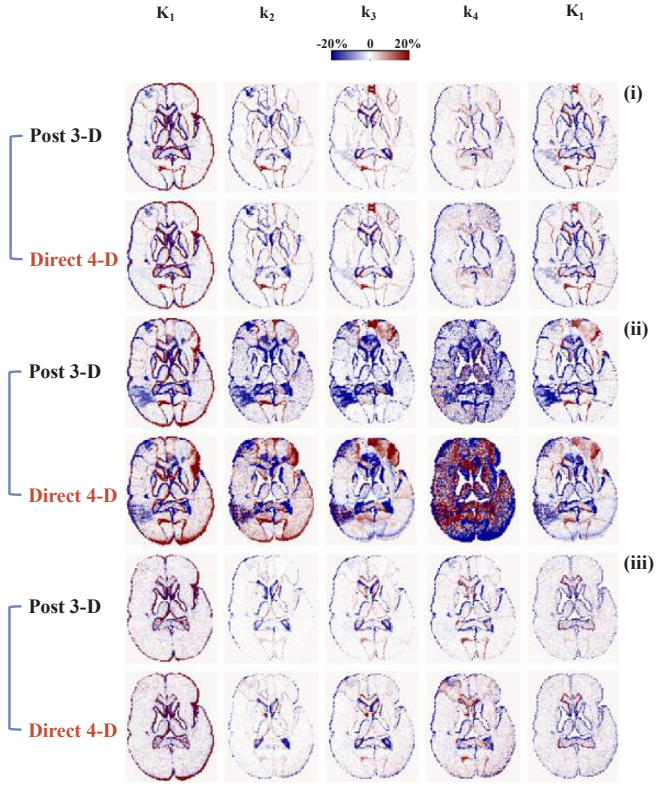

Fig. 7. Bias parametric maps for a representative slice through the [^{18}F]FDG brain phantom. Parameters are estimated both with post-reconstruction kinetic analysis and direct 4D image reconstruction and correspond to early frame motion with a 1-degree (i), 4-degree (ii), as well as a ± 2-degree rotation and returning to the original position (iii).

case represents mild motion, while the other one represents severe motion with increased rotations and translation even from the scan onset. This can be clearly seen in the severity of parameter bias with parameters in the severe motion case (Fig. 4(v)) being substantially more biased compared to the mild motion case (Fig. 4(vi)). Similar trends can be observed when parameters are estimated with direct 4D image reconstruction; but bias appears to be markedly higher in all kinetic parameters. This is particularly noticeable in the middle and late frame sudden motion patterns and both clinical studies. The increased bias appears to spatially propagate in the entire brain region and not only concentrated on the boundaries of regions with high intensity or kinetic parameter gradient. Similar to post-reconstruction analysis, parameter bias in the direct 4D reconstruction is shown to be related to the time point when motion was initiated, with k_4 been the most motion-sensitive parameter and heavily biased regardless of the pattern or initiation time point of head motion. On the other hand, Ki appears to be heavily biased when motion is initiated in the later stages during the course of the scan, something which is more often the case in dynamic brain imaging. Quantitative analysis in terms of whole brain kinetic parameter bias in Fig. 6 confirms the qualitative findings. When motion is initiated early during the scan, K_1 bias is the highest compared to when motion is initiated later on with bias at ~14% and ~17% for post-reconstruction and direct parameter estimation, respectively. Similarly bias in k_2 and k_3 is the highest when motion is initiated in the middle and late frames onwards and stands above ~20% and ~25%, respectively, in post-reconstruction analysis. The effect is even more pronounced with direct 4D reconstruction, with parameter bias peaking at above ~30% for k_2 and ~40% for k_3. Finally, k_4 is noticeably more biased compared to all parameters with a bias consistently above 45% regardless of motion pattern. However, it can be seen that k_4 bias peaks when motion is initiated late into the scan. Ki as it heavily depends on k_2 and k_3, which appear to be increasingly biased when motion is initiated towards the later part of the scan, it also follows the same pattern. K_1 and blood volume are the least biased parameters with bias consistently below ~20%. Comparing the 2 parameter estimation methods, it is also apparent that direct 4D reconstruction is more sensitive to inter-frame motion, with bias in all parameters being noticeably increased compared to post-reconstruction analysis. This increased sensitivity of direct 4D reconstruction under inter-frame motion can be more easily seen in Fig. 7 where parameter bias maps from early frame motion are seen, at increasing levels of motion, along with the corresponding quantitative analysis (Fig. 8).

For rotations below 2°, parameter bias is kept up to or below 10% across all parameters and with bias mainly concentrated in the boundaries of regions with different kinetics. Bias drops at even lower levels when the patient reverses back in the original position soon after the initial motion was initiated (Fig. 7 (iv)). At these bias levels, the 2 parameter estimation methods appear to be broadly similar with direct 4D showing slightly increased bias mainly in k_4. At 4° though, the bias in the post-reconstruction increased to well above 10% for all parameters and in the case of k_4 above 50%. At these bias levels, direct 4D reconstruction shows clear bias propagation compared to post-reconstruction analysis.

3.1.2. 1-tissue model

Similarly to Fig. 4, estimated kinetic parameters from the [^{15}O]H_2O datasets along with the corresponding parametric bias maps for a subset of the simulated motion patterns, are shown in Fig. 9. As seen in the dynamic [^{18}F]FDG data, the bias amongst parameters is dependent upon the time point of motion initiation with k_2 bias increasing going towards late temporal initiation of motion (Fig. 9(i–iii)).

The volume of distribution follows a similar pattern with bias peaking at 10% after 10 iterations when early motion is initiated, compared to more than 20% when motion occurs towards the end of the scan duration (Fig. 10). On the other hand, K_1 is more affected when motion is initiated early on during the scan with a ~17% bias. Comparing the parameter estimation methods, direct 4D reconstruction again appears to be more sensitive to inter-frame motion. Such effect is more pronounced in the 2 cases simulating clinically observed motion levels, where parameter bias is generally higher. Looking again at the parameter bias following early frame motion and at increasing rotation levels (Figs. 11 and 12), both parameter estimation methods look very closely matched. Even though, the bias increases progressively at increasing levels of rotation, it is kept < 15% for K_1 and < 10% for the rest of parameters.

3.2. Noisy data

Similar analysis was performed under noisy conditions for a subset of the motion patterns as defined in the *Methods* section. When noise is considered, parameter estimation is affected not only by motion artefacts, but also by statistical noise, which makes it very challenging to attribute the observed bias to any of these 2 effects. Looking at the bias parametric maps in Fig. 13, it can be seen that k_4 again remains the least robust parameter to estimate under the presence of combined noise and motion-induced bias. However, looking across the different motion patterns, the noise-induced bias appears to be the largest contributor to kinetic parameter bias compared to any bias attributed to motion looking at the noiseless data, since parameter bias across all motion patterns shows little difference. The quantitative analysis (Fig. 14) confirms this trend with little to choose amongst the different motion patterns. Comparing the Ki noiseless and noisy cases, we can see the bias going from < 20% to more than 75% for both kinetic parameter estimation methods, confirming the fact that the largest proportion of bias originates from noise in the data. However, in contrast to noiseless data where direct 4D reconstruction appears more biased compared to post-reconstruction analysis, under noisy conditions, the

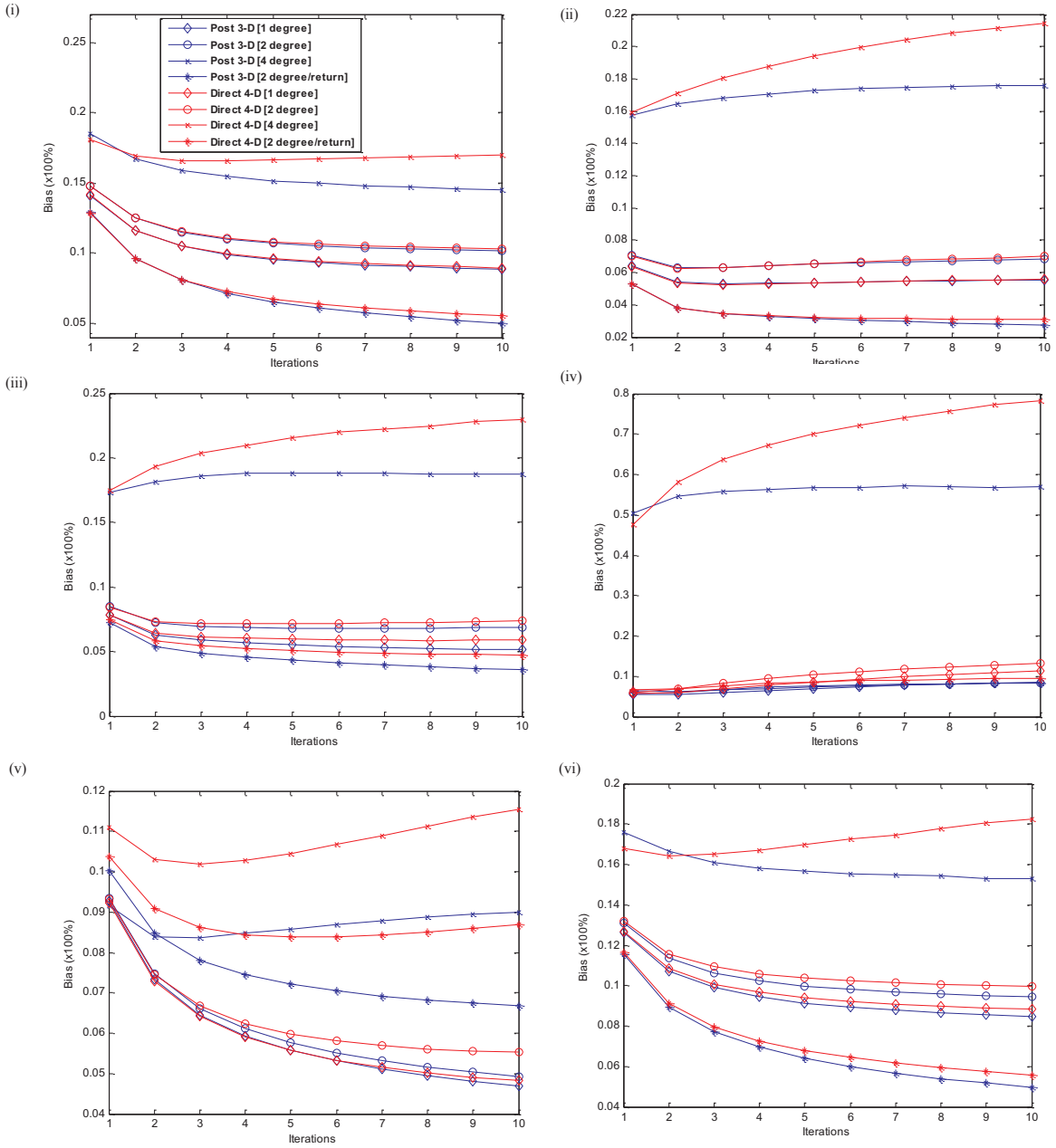

Fig. 8. Whole brain kinetic parameter bias from [^{18}F]FDG noiseless data for K_1 (i), k_2 (ii), k_3 (iii), k_4 (iv), blood volume (v) and K_i (vi) at increasing levels of early frame motion. Parameters are estimated both with post-reconstruction kinetic analysis and direct 4D image reconstruction.

superiority of the direct 4D methodology is able to counterbalance any deficit due to propagation in all parameters other than K_1 and k_4 (and even in those both estimation methods appear to be within 5%). On the other parameters, the bias in 4D reconstruction appears to be reduced on average and amongst motion patterns, by more than ~15% in k_2 and k_3 and ~7% on blood volume and Ki, compared to post-reconstruction analysis. Similar behaviour can be seen on the [^{15}O]H_2O datasets with k_2, blood volume and Vd bias being more pronounced compared to K_1 amongst all simulated motion patterns (Fig. 15). Again little difference can be seen amongst the different motion patterns in Fig. 16 as noise-induced bias appears to contribute to a large extent to the observed parameter bias compared to any motion-induced bias. However, again direct 4D reconstructed parameters appear less biased apart from K_1 in which post-reconstruction has a reduced bias by ~9%.

To obtain an overview of the differences between the 2 parameter estimation methods, bias and coefficient of variation parametric maps are shown in Fig. 17 and Fig. 18, respectively, for Ki (2-tissue model) and Vd (1-tissue model) using both parameter estimation methods and for the different motion patterns. Comparing bias and variance under no motion to all simulated motion cases, little difference can be seen in most of the regions. Thus under noisy conditions most of bias or variance in the parameters can be attributed to statistical noise in the data compared to bias or variance originating from any inter-frame motion. Bias and variance amongst regions vary especially to regions which are in the vicinity of other regions with significantly activity gradients. To better visualize the relative impact of motion and noise on regional parameter bias under both noiseless and noisy data, scatter plots for all 83 regions in the phantom are shown in Fig. 19 corresponding again to Vd and Ki and using the severe clinically-observed simulated motion pattern. Under noiseless condition, both Ki and Vd estimated with both

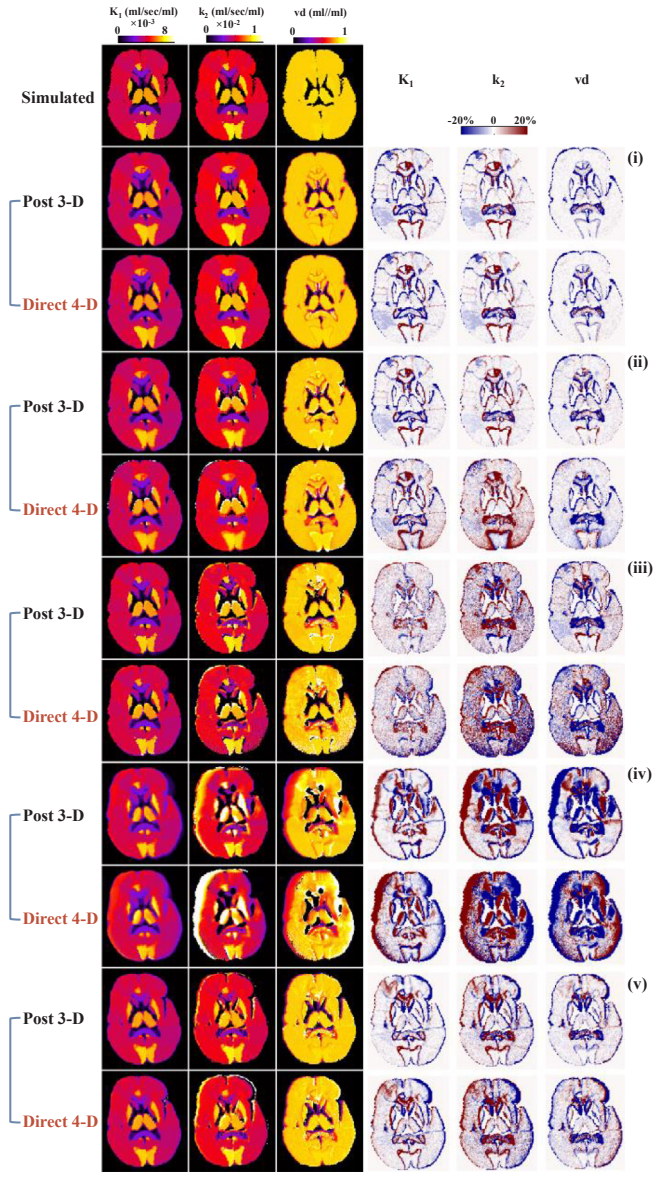

Fig. 9. Simulated and estimated kinetic parameters from noiseless data along with the corresponding bias parametric maps for a representative slice through the $[^{15}O]H_2O$ brain phantom. Parameters are estimated both with post-reconstruction kinetic analysis and direct 4D image reconstruction and correspond to early (i), middle (ii) and late frame (iii) motion with a 4-degree rotation, as well as a representative severe (iv) and mild (v) patient motion pattern.

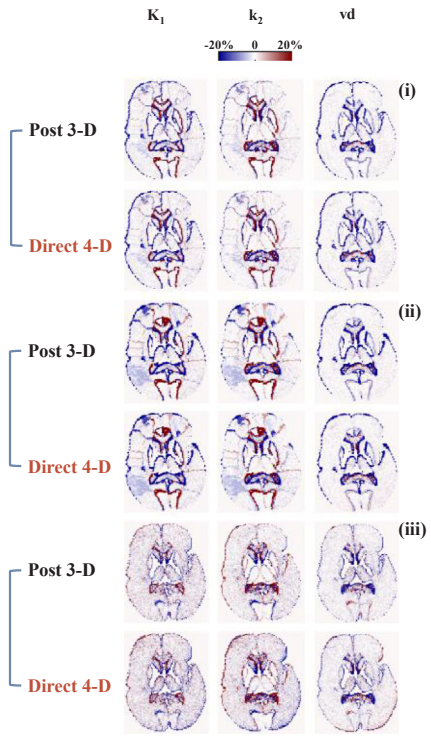

Fig. 11. Bias parametric maps for a representative slice through the noiseless $[^{15}O]H_2O$ brain phantom. Parameters are estimated both with post-reconstruction kinetic analysis and direct 4D image reconstruction and correspond to early frame motion with a 1-degree (i), 4-degree (ii), as well as a ± 2-degree rotation and returning to the original position (iii).

parameter estimation methods are negatively biased (Figs. 4(v) and 9(v)). The regression of K_i amongst all regions estimated with direct 4D reconstruction is further biased compared to post-reconstruction analysis, while on the Vd both methods are closely matched. This is due to the additional propagation of bias, as observed in Figs. 6(iv) and 10(iii). Going to noisy data, bias in the parameters becomes even more pronounced as bias originates not only from motion but most importantly from noise in the data. However, direct 4D estimated parameters are clearly less biased both for Vd and Ki. Therefore, despite any deficit due to error propagation, under noisy conditions the direct approach to parameter estimation still outperforms traditional post-reconstruction analysis, even under severe inter-frame motion. This is attributed to the fact that direct 4D reconstruction can estimate less noisy dynamic data leading to less noisy kinetic parameters. Thus the additional error propagation from inter-frame motion is not sufficient to render direct 4D reconstruction more biased compared to post-reconstruction

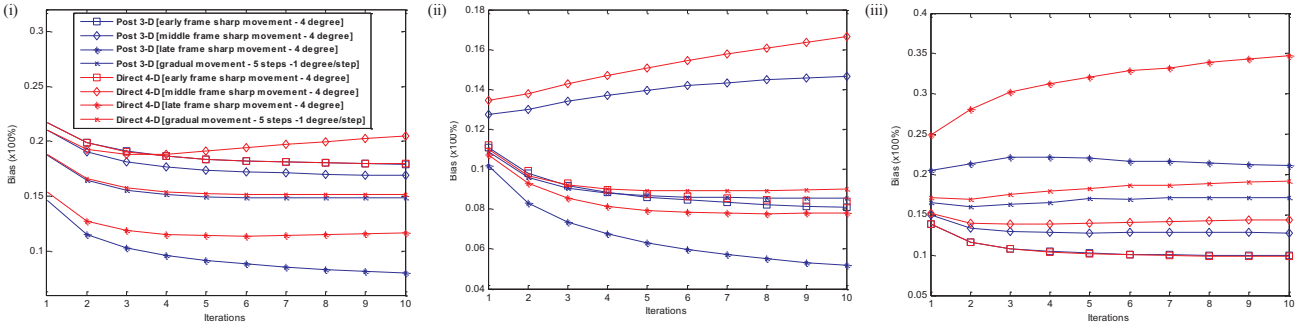

Fig. 10. Whole brain kinetic parameter bias from $[^{15}O]H_2O$ noiseless data for K_1 (i), blood volume (ii) and Vd (iii) at high levels of early, middle and late frame motion as well as during slow continuous drift. Parameters are estimated both with post-reconstruction kinetic analysis and direct 4D image reconstruction.

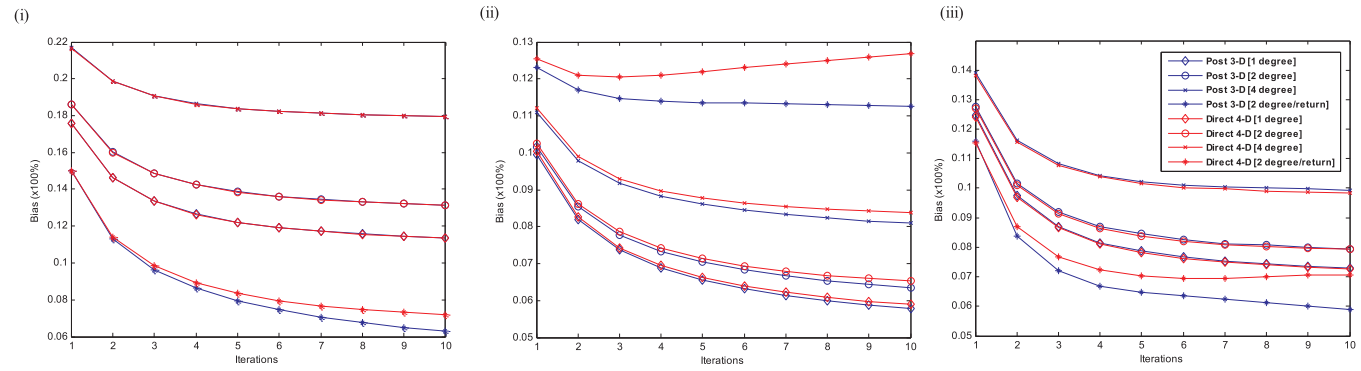

Fig. 12. Whole brain kinetic parameter bias from [^{15}O]H_2O noiseless data for K_1 (i), blood volume (ii) and Vd (iii) at increasing levels of early frame motion. Parameters are estimated both with post-reconstruction kinetic analysis and direct 4D image reconstruction.

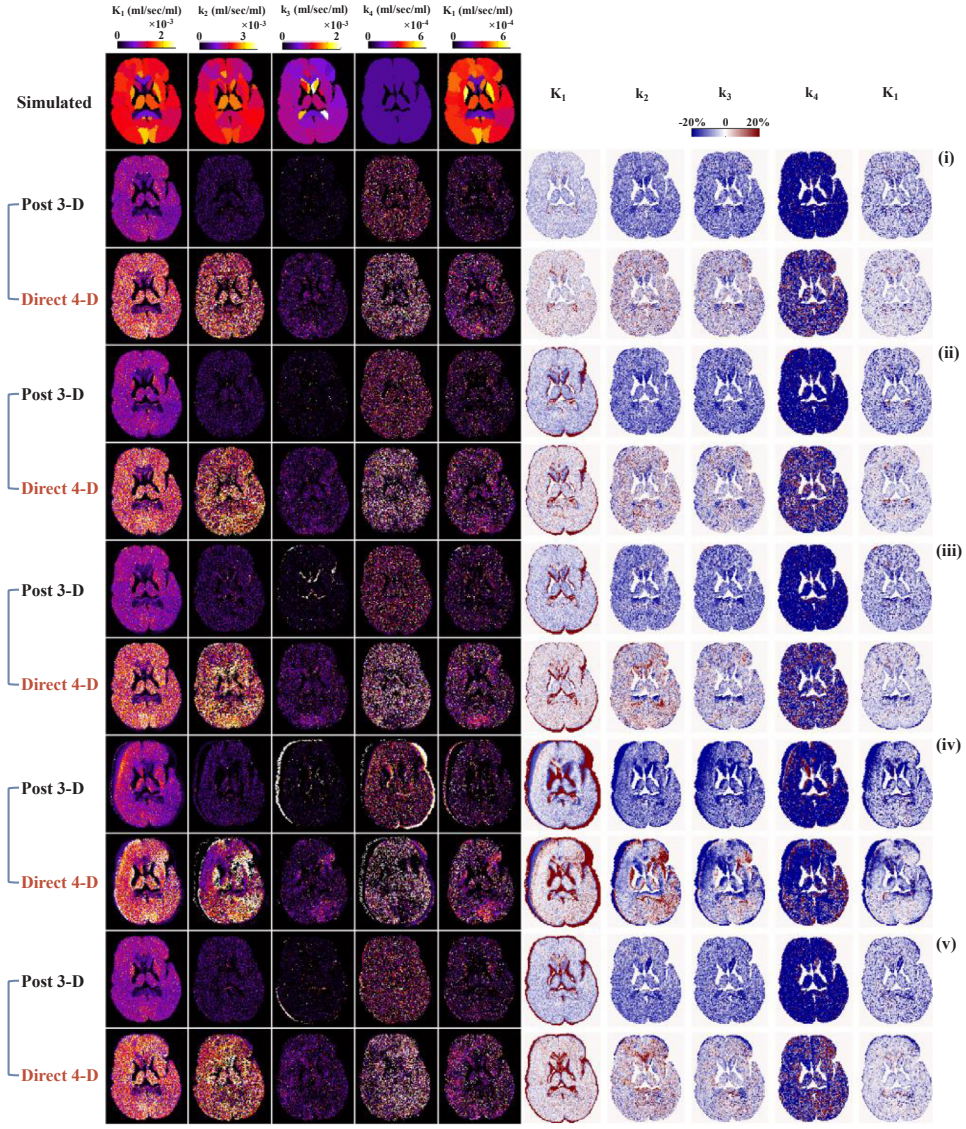

Fig. 13. Simulated and estimated kinetic parameters from noisy data along with the corresponding bias parametric maps for a representative slice through the [^{18}F] FDG brain phantom. Parameters are estimated both with post-reconstruction kinetic analysis and direct 4D image reconstruction and correspond to early (i), middle (ii) and late frame (iii) motion with a 4-degree rotation, as well as a representative severe (iv) and mild (v) patient motion pattern.

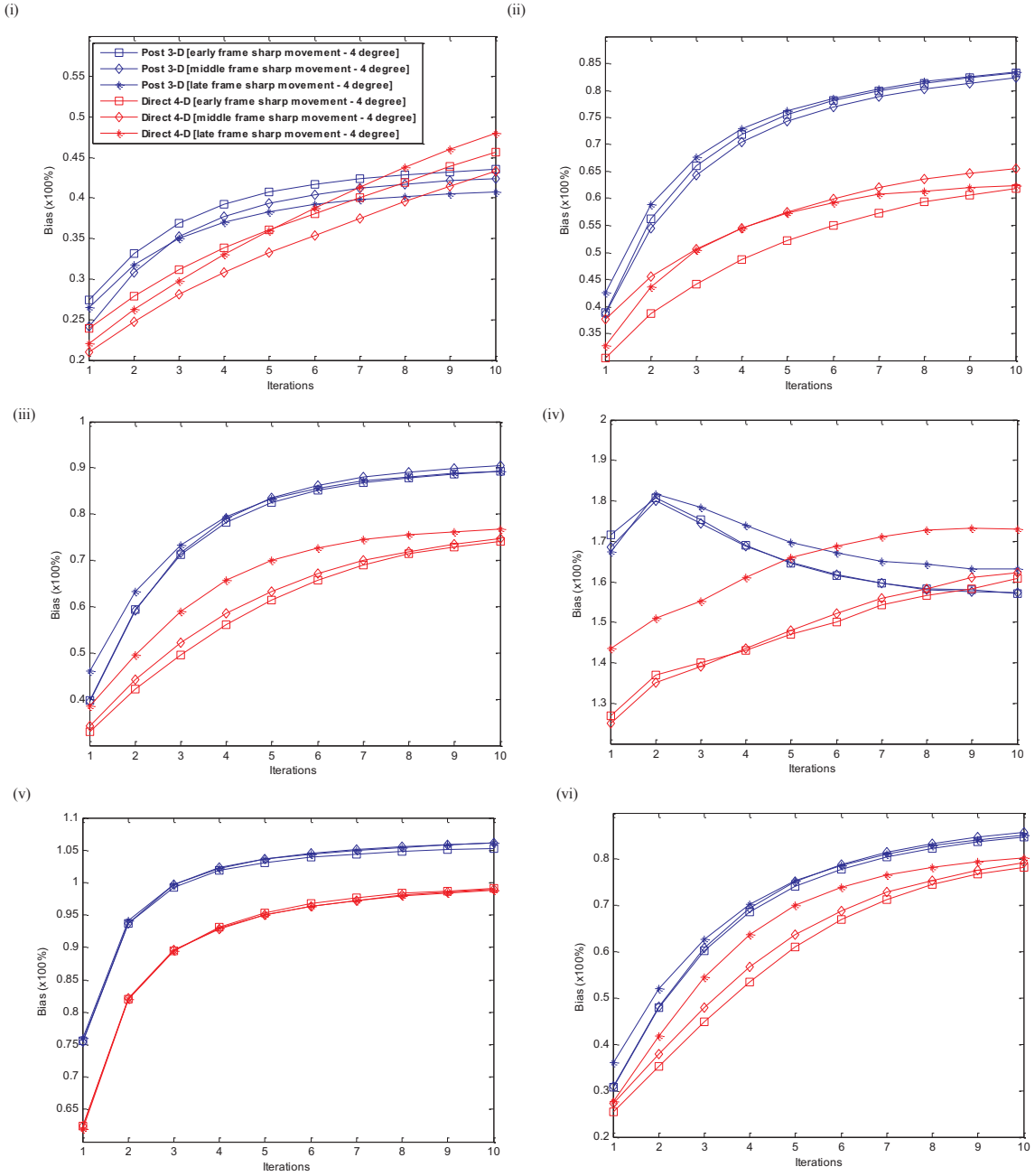

Fig. 14. Whole brain kinetic parameter bias from [^{18}F]FDG noisy data for K_1 (i), k_2 (ii), k_3 (iii), k_4 (iv), blood volume (v) and K_i (vi) at high levels of early, middle and late frame motion. Parameters are estimated both with post-reconstruction kinetic analysis and direct 4D image reconstruction.

analysis which doesn't suffer from error propagation but is more susceptible to noise-induced kinetic parameter bias.

4. Discussion

Dynamic neuro-receptor and generally brain PET imaging often involves kinetic parameter estimation of fine anatomical structures. Current dedicated brain PET scanners offer the possibility of obtaining voxel-wise parametric maps of micro- and macro- parameters at high spatial resolution, thus making the probing of functional information from such small brain structures feasible. However, due to a number of reasons, voluntary and involuntary head motion can inadvertently produce non-physiologic variations in the voxel-wise and regional time activity curves leading to erroneous kinetic parameter estimates and potentially misleading clinical outcomes. Therefore, in the absence of motion correction schemes during data analysis or in the presence residual motion following motion correction, it is important to characterize the robustness of kinetic parameters under various motion and kinetic modelling related parameters, such as the level of motion, its temporal initiation, as well as the kinetic parameter estimation method.

The analysis of both 1-tissue and 2-tissue models suggests that different parameters are affected to a different extend depending on the time the voluntary or involuntary motion occurred. In both tissue models used in this study, parameter bias appears to be more severe when initiated towards the late stages of the scan. This is of importance since in most clinical cases motion takes place towards the end of the scan due to fatigue and aches from the prolonged immobilisation. For the [^{18}F]FDG datasets, k_4 was proven to be the most sensitive parameter regardless at which time point the motion was initiated. On the other hand, on the [^{15}O]H_2O datasets, k_2 was found to be sensitive to

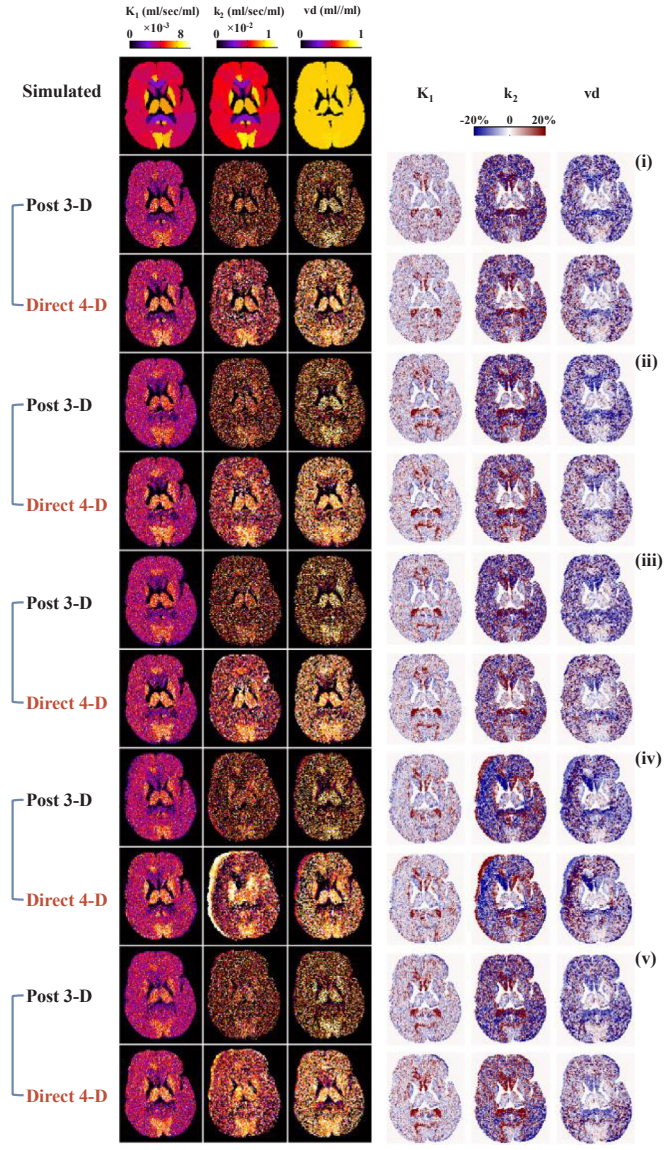

Fig. 15. Simulated and estimated kinetic parameters from noisy data along with the corresponding bias parametric maps for a representative slice through the $[^{15}O]H_2O$ brain phantom. Parameters are estimated both with post-reconstruction kinetic analysis and direct 4D image reconstruction and correspond to early (i), middle (ii) and late frame (iii) motion with a 4-degree rotation, as well as a representative severe (iv) and mild (v) patient motion pattern.

movement, though on average the biases observed on the 1-tissue model are less than those observed on the 2-tissue model under similar motion level. The number of parameters to estimate in both models may contribute to the robustness of each kinetic parameter to potential motions during the course of the scan similar to the effect under statistical noise. Another reason might be the kinetic parameter variation amongst the 83 regions, since for the $[^{15}O]H_2O$ data the simulated parameters used, produce less steep uptake gradients, therefore resulting in less bias in the boundaries between regions. In both models, when the patient returned to the initial position following a movement, greatly reduced the parameter bias compared to if the patient had stayed permanently to a new position following an initial movement. Furthermore, slow drift happening during the course of the scan produced less parameter bias as opposed to sudden changes in head posture.

Comparing across the 2 parameter estimation methods, different levels of bias were observed. In accordance with our previous observations [24], direct parameter estimation resulted in additional bias. The increased bias in the direct 4D reconstruction appears to be related to the level of bias seen in the post-reconstruction analysis therefore potentially signifying propagation of bias between the tomographic and kinetic modelling steps. As shown in Fig. 7, when the level of motion is small and the amount of bias in the post-reconstruction analysis is kept low, the direct 4D estimated parameters match the ones from post-reconstruction analysis. However as the level of motion is increased and parameters become more biased in the post-reconstruction analysis, additional bias is apparent in the 4D reconstruction, something that is of importance when selecting the direct method to parameter estimation. Crucially though under noisy conditions direct 4D reconstruction substantially reduces bias compared to post-reconstruction analysis despite the additional bias due to bias propagation originating from motion. Furthermore, bias differences amongst different motion patterns are small when compared to the level of bias due to noise, though bias propagation due to motion reduces the full benefits of direct 4D reconstruction in the presence of statistical noise. It is also expected that bias propagation due to motion becomes more pronounced at increasing levels of injected dose or improved counting statistics as bias due to noise and the benefits of 4D reconstruction under statistical noise are expected to be reduced. Such an effect is even more pronounced if the effects of emission/attenuation mismatch are taken also into account, thus increasing the overall bias due to inter-frame motion. Such an effect can be seen in Fig. 18 for the mild clinically-observed simulated motion pattern both for K_1 and Vd, representing macro-parameters from both 1- and 2-tissue models. The addition of emission/attenuation mismatch adds to the overall bias though the additional bias is less than 4% for both parameters and most of the bias originates from the emission blurring (Fig. 20). However, such a trend might be dependent upon the simulated parameters used in this study as kinetic

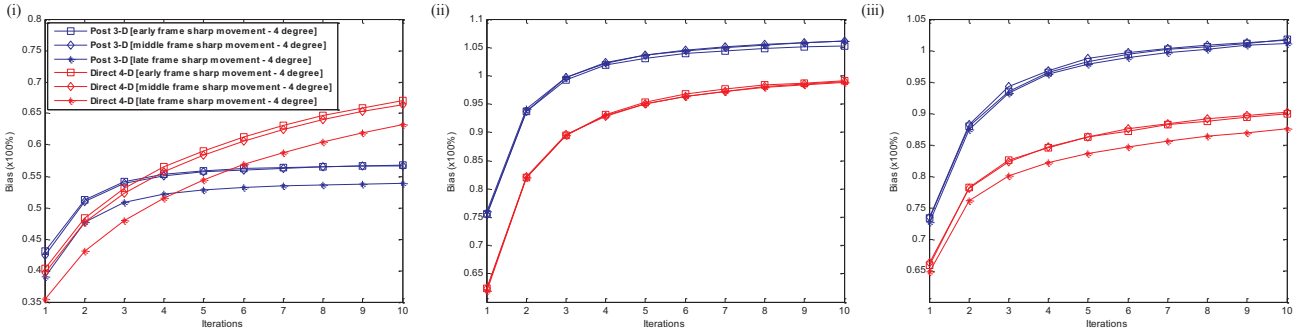

Fig. 16. Whole brain kinetic parameter bias from $[^{15}O]H_2O$ noisy data for K_1 (i), blood volume (ii) and Vd (iii) at high levels of early, middle and late frame motion. Parameters are estimated both with post-reconstruction kinetic analysis and direct 4D image reconstruction.

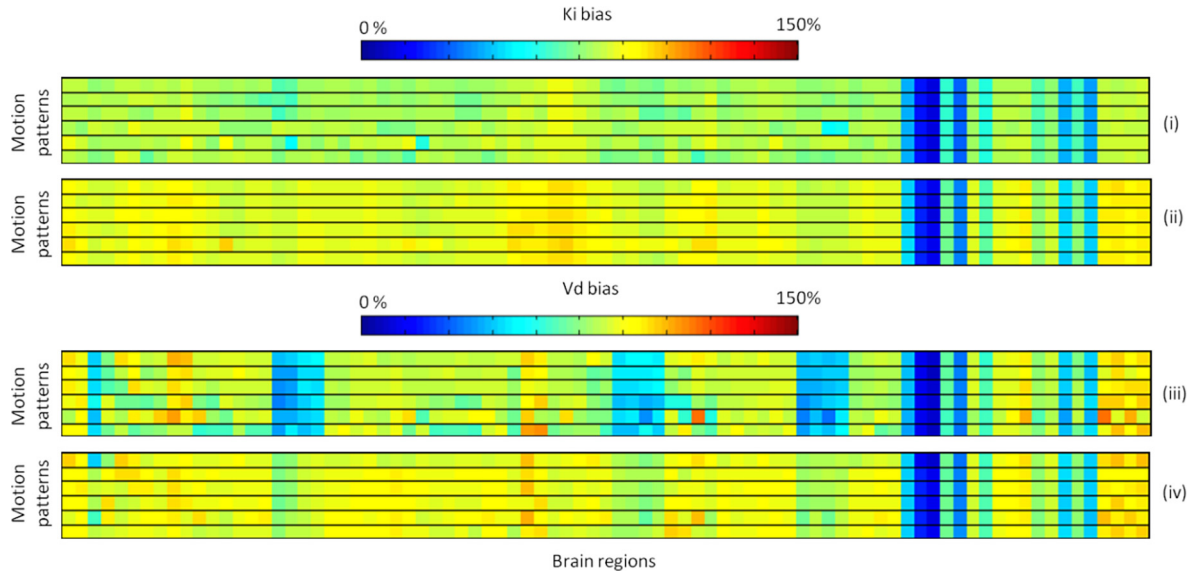

Fig. 17. Regional bias parametric maps of Ki (i, ii) and Vd (iii, iv) for each of the 83 regions in the phantom for 6 different motion patterns (from the top: no motion, 4° early frame movement, 4° middle frame movement, 4° late frame movement as well as severe and mild patient movement). Parameter bias is shown both for post-reconstruction kinetic analysis (ii, iv) and direct 4-D image reconstruction (i, iii).

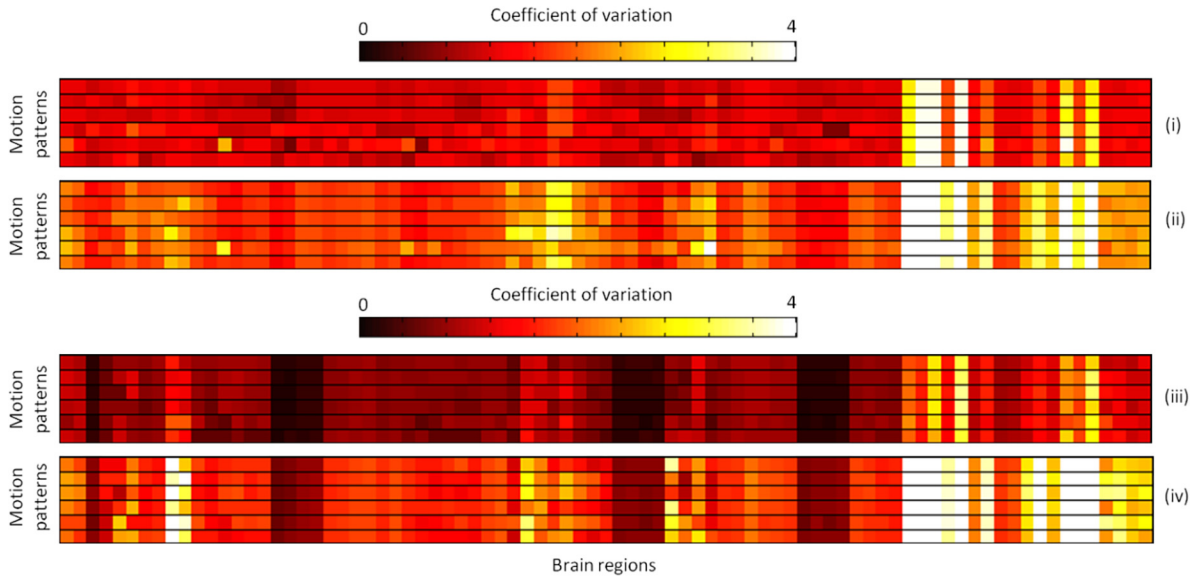

Fig. 18. Regional coefficient of variation parametric maps of Ki (i, ii) and Vd (iii, iv) for each of the 83 regions in the phantom for 6 different motion patterns (from the top: no motion, 4° early frame movement, 4° middle frame movement, 4° late frame movement as well as severe and mild patient movement). Parameter bias is shown both for post-reconstruction kinetic analysis (ii, iv) and direct 4-D image reconstruction (i, iii).

parameter variation amongst regions might be larger than any variations in the attenuation factors. Therefore, the inter-frame motion-induced bias due to emission blurring might be more pronounced than due to attenuation mismatch.

In this study the simulated phantom included only white and grey matter structures, ignoring bony structures and cerebrospinal fluid (CSF). Therefore, the gradient in emission/attenuation of the bony region and CSF, compared to the brain, could further accentuate any bias observed in the current study. Such emission/attenuation mismatch will also affect scatter estimation and correction [33,34], though the current study did not include any effects from erroneous scatter estimation. We also opted to simulate representative motion patterns in a systematic way as well as using representative clinically observed motion patterns. However, a variety of motion patterns can be encountered in clinical practice with respect to the time of motion initiation and the severity of motion, which can alter the obtained kinetic parameter bias. Usually motion can be encountered at later time points during the course of the scan ($t > 10$ min). However, it is not uncommon to encounter early head motion, particularly sudden position changes for the reasons elaborated earlier. Therefore, despite the short scan duration of a dynamic [^{15}O]H_2O scan, motion is still likely to take place, especially in patients with neurological disorders. Furthermore, if repeated [^{15}O]H_2O scans are performed (e.g. in activation studies), then motion due to fatigue or body aches becomes also more likely to occur.

We investigated 1-tissue and 2-tissue models based on [^{15}O]H_2O and [^{18}F]FDG kinetics. However, using other tracers with higher or lower uptake variation within brain structures could alter the kinetic parameter bias both in post-reconstruction analysis and direct 4D reconstruction. Higher kinetic parameter gradient amongst different brain regions could accentuate TAC errors in the boundaries of regions under inter-frame motion. This in turn could also accentuate additional error propagation when parameters are directly estimated. Such an

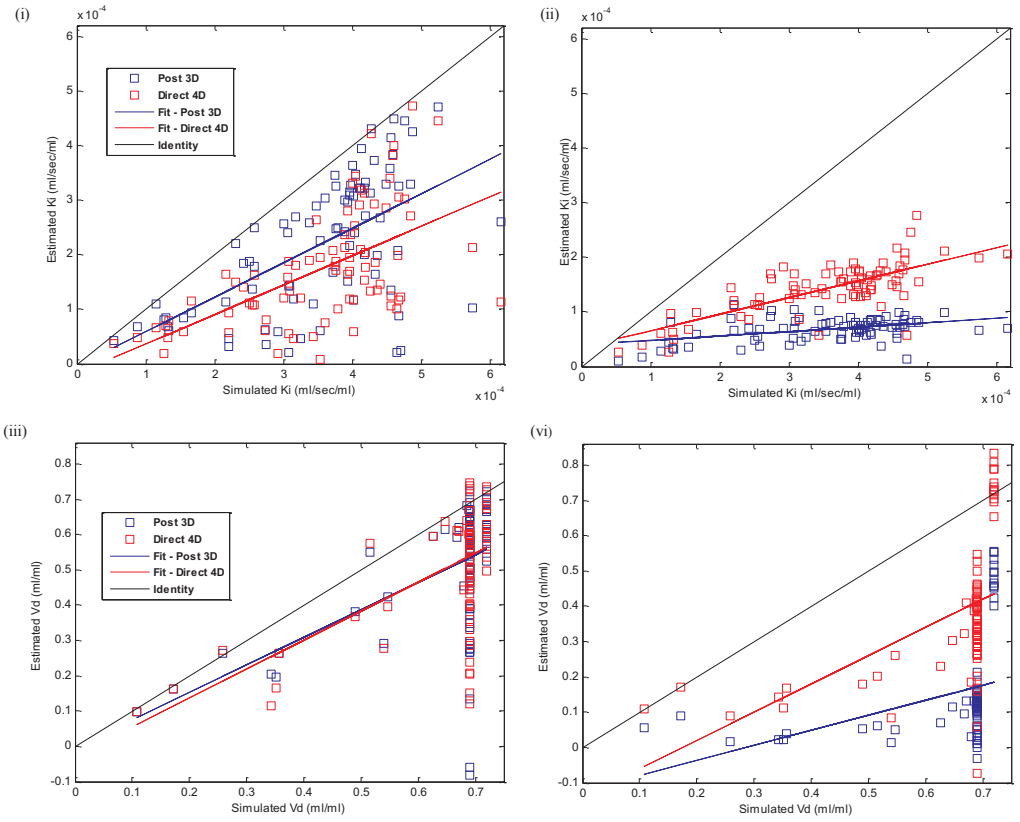

Fig. 19. Regional kinetic parameter bias scatter plots for K_i (i, ii) and Vd (iii, iv) for all 83 regions within the brain phantom for the severe clinically-observed simulated motion pattern. Data are shown both for noiseless (i, iii) and noisy (ii, iv) simulations and parameter estimation performed both with post-reconstruction kinetic analysis and direct 4D image reconstruction.

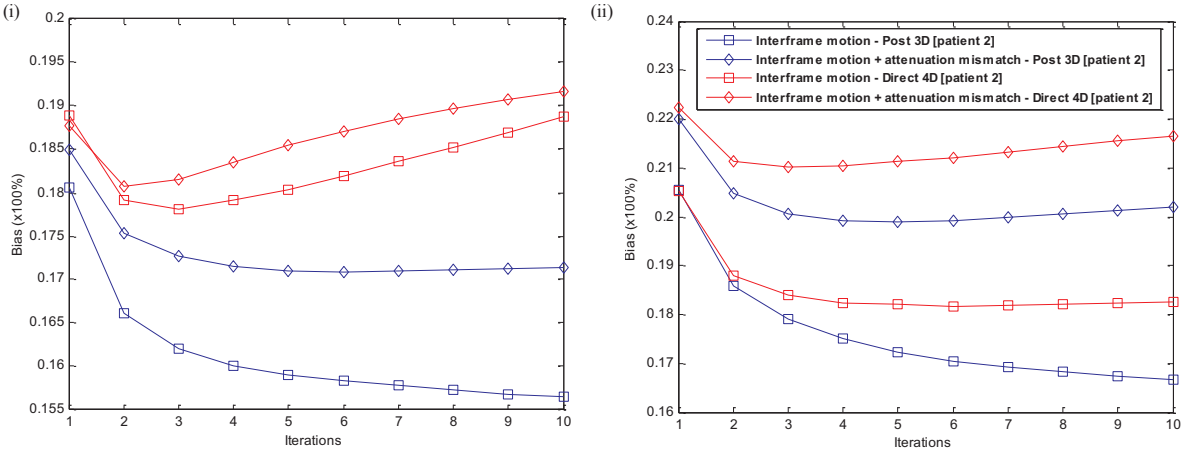

Fig. 20. Whole brain K_i (i) and Vd (ii) kinetic parameter bias from [^{18}F]FDG (i) and [^{15}O]H_2O (ii) noiseless data derived by simulating a mild patient motion pattern. Kinetic parameter bias is compared using inter-frame motion only and combined inter-frame motion and attenuation mismatch for both with post-reconstruction kinetic analysis and direct 4D image reconstruction.

effect is tracer-specific, therefore for tracers exhibiting high specific uptake in certain regions, motion-induced bias and its propagation within 4D reconstruction could be more detrimental. Under such conditions, motion correction using either frame-by-frame methods or image reconstruction-based methods is highly recommended, especially when the protocol involves direct parameter estimation within a unified image reconstruction and kinetic modelling framework. In the absence of a motion correction scheme, motion-induced bias propagation could be limited by means of a time-of-flight based direct 4D image reconstruction [24]. However, bias reduction seen in thoracic and abdominal imaging can only be realized at substantially higher TOF time resolutions due to the difference in the diameter of the scanned object. Until such time resolutions become available, accurate motion correction schemes are important to realize the benefits of direct 4D image reconstruction for improved parameter estimation.

A natural extension of this work would be to investigate the impact of motion mitigation techniques also considering neuro-receptor studies involving simplified analysis. These can include motion correction

during or after image reconstruction as well as temporal frame omission in those frames in which motion has occurred and in the absence of any motion correction algorithm. In fact, it is of interest to investigate whether omitting entire frames in which the patient moved and returned subsequently in his original position, can mitigate the effects of motion. In cases where motion occurs early during the scan, where kinetics change rapidly, omitting entire frames might result in biased kinetic parameters. However, if motion occurs towards the end of the scan, in which kinetics are slower, then frame omission might be an alternative method in case motion correction algorithms are not available. Nevertheless, if motion correction algorithms are available, they should be the method of choice even in case where motion correction might not work optimally.

5. Conclusion

Inter-frame motion in dynamic neuro-receptor and brain PET imaging is a substantial source of kinetic parameter bias. Using a number of motion patterns encountered in clinical practice, it was demonstrated that such parameter bias depends not only on the severity of motion but also on the temporal frame of its occurrence. Additionally, post-reconstruction parameter estimation is less susceptible to motion errors compared to direct parameter estimation within image reconstruction, which suffers from additional bias through propagation of errors. Despite such a penalty, direct 4D image reconstruction produces more accurate and robust pharmacokinetic parameters under noisy conditions, though its benefits become potentially less apparent at increasing levels of inter-frame motion or decreasing levels of statistical noise. Therefore, it is recommended that motion correction schemes are included as part of the kinetic modelling parameter estimation process, especially in cases when direct approaches are used for generating voxel-wise pharmacokinetic parametric maps.

Acknowledgments

This work was supported by the Swiss National Science Foundation under Grant SNSF 320030_176052 and the Swiss Cancer Research Foundation under Grant KFS-3855-02-2016.

Conflict of interest

The authors have no relevant conflicts of interest to disclose.

Appendix A. Supplementary data

Supplementary data associated with this article can be found, in the online version, at https://doi.org/10.1016/j.ejmp.2018.08.006.

References

[1] Mohy-ud-Din H, Karakatsanis NA, Willis W, Tahari AK, Wong DF, Rahmim A. Intra-frame motion compensation in multi-frame brain PET imaging. Front Biomed Technol 2015;2:366–79.
[2] Ruttimann UE, Andreason PJ, Rio D. Head motion during positron emission tomography: is it significant? Psychiatry Res 1995;61:43–51.
[3] Green MV, Seidel J, Stein SD, Tedder TE, Kempner KM, Kertzman C, et al. Head movement in normal subjects during simulated PET brain imaging with and without head restraint. J Nucl Med 1994;35:1538–46.
[4] Bloomfield PM, Spinks TJ, Reed J, Schnorr L, Westrip AM, Livieratos L, et al. The design and implementation of a motion correction scheme for neurological PET. Phys Med Biol 2003;48:959–78.
[5] Wong DF, Brasic JR, Singer HS, Schretlen DJ, Kuwabara H, Zhou Y, et al. Mechanisms of dopaminergic and serotonergic neurotransmission in Tourette syndrome: clues from an in vivo neurochemistry study with PET. Neuropsychopharmacology 2008;33:1239–51.
[6] Lopresti BJ, Russo A, Jones WF, Fisher T, Crouch DG, Altenburger DE, et al. Implementation and performance of an optical motion tracking system for high resolution brain PET imaging. IEEE Trans Nucl Sci 1999;46:2059–67.
[7] Jin X, Mulnix T, Gallezot J-D, Carson RE. Evaluation of motion correction methods in human brain PET imaging—A simulation study based on human motion data. Med Phys 2013;40:102503.
[8] Dinelle K, Ngo H, Blinder S, Vafai N, Topping G, Sossi V. Frame-to-frame image realignment assessment tool for dynamic brain positron emission tomography. Med Phys 2011;38:773–81.
[9] Olesen OV, Paulsen RR, Hojgaard L, Roed B, Larsen R. Motion tracking for medical imaging: a nonvisible structured light tracking approach. IEEE Trans Med Imaging 2012;31:79–87.
[10] Rahmim A, Rousset O, Zaidi H. Strategies for Motion Tracking and Correction in PET. PET Clinics 2007;2:251–66.
[11] Rahmim A, Dinelle K, Cheng J-C, Shilov MA, Segars WP, Lidstone SC, et al. Accurate event-driven motion compensation in high-resolution PET incorporating scattered and random events. IEEE Trans Med Imaging 2008;27:1018–33.
[12] Qiao F, Pan T, Clark Jr JW, Mawlawi OR. A motion-incorporated reconstruction method for gated PET studies. Phys Med Biol 2006;51:3769–83.
[13] Wardak M, Wong K-P, Shao W, Dahlbom M, Kepe V, Satyamurthy N, et al. Movement Correction Method for Human Brain PET Images: Application to Quantitative Analysis of Dynamic 18F-FDDNP Scans. J Nucl Med 2010;51:210–8.
[14] Costes N, Dagher A, Larcher K, Evans AC, Collins DL, Reilhac A. Motion correction of multi-frame PET data in neuroreceptor mapping: simulation based validation. NeuroImage. 2009;47:1496–505.
[15] Mourik JM, Lubberink M, van Velden FP, Lammertsma A, Boellaard R. Off-line motion correction methods for multi-frame PET data. Eur J Nucl Med Mol Imaging 2009;36:2002–13.
[16] Ye H, Wong KP, Wardak M, Dahlbom M, Kepe V, Barrio JR, et al. Automated movement correction for dynamic PET/CT images: evaluation with phantom and patient data. PLoS One 2014;9:e103745.
[17] Jiao J, Searle GE, Schnabel JA, Gunn RN. Impact of image-based motion correction on dopamine D3/D2 receptor occupancy—comparison of groupwise and frame-by-frame registration approaches. EJNMMI Phys 2015;2:15.
[18] Keller SH, Sibomana M, Olesen OV, Svarer C, Holm S, Andersen FL, et al. Methods for Motion Correction Evaluation Using 18F-FDG Human Brain Scans on a High-Resolution PET Scanner. J Nucl Med 2012;53:495–504.
[19] Herzog H, Tellmann L, Fulton R, Stangier I, Rota Kops E, Bente K, et al. Motion artifact reduction on parametric PET images of neuroreceptor binding. J Nucl Med. 2005;46:1059–65.
[20] Mourik JE, Lubberink M, Lammertsma AA, Boellaard R. Image derived input functions: effects of motion on tracer kinetic analyses. Mol Imaging Biol. 2011;13:25–31.
[21] Gravel P, Reader AJ. Direct 4D PET MLEM reconstruction of parametric images using the simplified reference tissue model with the basis function method for [(1)(1)C]raclopride. Phys Med Biol 2015;60:4533–49.
[22] Angelis G, Matthews J, Kotasidis F, Markiewicz P, Lionheart W, Reader A. Evaluation of a direct 4D reconstruction method using generalised linear least squares for estimating nonlinear micro-parametric maps. Ann Nucl Med 2014;1–14.
[23] Reader AJ, Verhaeghe J. 4D image reconstruction for emission tomography. Phys Med Biol 2014;59:R371–418.
[24] Kotasidis FA, Mehranian A, Zaidi H. Impact of time-of-flight on indirect 3D and direct 4D parametric image reconstruction in the presence of inconsistent dynamic PET data. Phys Med Biol 2016;61:3443–71.
[25] Hammers A, Allom R, Koepp MJ, Free SL, Myers R, Lemieux L, et al. Three-dimensional maximum probability atlas of the human brain, with particular reference to the temporal lobe. Hum Brain Mapp 2003;19:224–47.
[26] Gousias IS, Rueckert D, Heckemann RA, Dyet LE, Boardman JP, Edwards AD, et al. Automatic segmentation of brain MRIs of 2-year-olds into 83 regions of interest. NeuroImage. 2008;40:672–84.
[27] Dinelle K, Blinder S, Cheng JC, Lidstone S, Buckley K, Ruth TJ, et al. Investigation of Subject Motion Encountered During a Typical Positron Emission Tomography Scan. 2006 IEEE Nuclear Science Symposium Conference Record. p. 3283-7.
[28] Woods RP, Grafton ST, Holmes CJ, Cherry SR. Mazziotta JC. Automated image registration: I. General methods and intrasubject, intramodality validation. J Comput Assist Tomogr. 1998;22:139–52.
[29] Mukherjee JM, Lindsay C, Mukherjee A, Olivier P, Shao L, King MA, et al. Improved frame-based estimation of head motion in PET brain imaging. Med Phys. 2016;43:2443–54.
[30] Mehranian A, Kotasidis F, Zaidi H. Accelerated time-of-flight (TOF) PET image reconstruction using TOF bin subsetization and TOF weighting matrix pre-computation. Phys Med Biol. 2016;61:1309–31.
[31] Matthews JC, Angelis GI, Kotasidis FA, Markiewicz PJ, Reader AJ. Direct reconstruction of parametric images using any spatiotemporal 4D image based model and maximum likelihood expectation maximisation. IEEE Nucl Sci Symp Conf Rec (NSS/MIC) 2010:2435–41.
[32] Feng D, Huang SC, ZhiZhong W, Dino H. An unbiased parametric imaging algorithm for nonuniformly sampled biomedical system parameter estimation. IEEE Trans Med Imaging 1996;15:512–8.
[33] Anton-Rodriguez JM, Sibomana M, Walker MD, Huisman MC, Matthews JC, Feldmann M, et al. Investigation of motion induced errors in scatter correction for the HRRT brain scanner. IEEE Nucl Sci Symp Conf Rec (NSS/MIC) 2010:2935–40.
[34] Mansor S, Boellaard R, Huisman MC, van Berckel BN, Schuit RC, Windhorst AD, et al. Impact of new scatter correction strategies on High-Resolution Research Tomograph brain PET studies. Mol Imaging Biol 2016;18:627–35.